Available online at www.sciencedirect.com
ScienceDirect
Journal of the European Ceramic Society 29 (2009) 91–98
www.elsevier.com/locate/jeurceramsoc

Densification of nanocrystalline Y_2O_3 ceramic powder by spark plasma sintering

Rachman Chaim [a,*], Amit Shlayer [a], Claude Estournes [b]

[a] *Department of Materials Engineering, Technion – Israel Institute of Technology, Haifa, Israel*
[b] *Institut Carnot CIRIMAT, UMR CNRS-UPS-INP 5085, Bat. 2R1, Universite Paul Sabatier, 31062 Toulouse Cedex 9, France*

Received 25 January 2008; received in revised form 12 May 2008; accepted 17 May 2008
Available online 17 July 2008

Abstract

Nanocrystalline Y_2O_3 powders with 18 nm crystallite size were sintered using spark plasma sintering (SPS) at different conditions between 1100 and 1600 °C. Dense specimens were fabricated at 100 MPa and 1400 °C for 5 min duration. A maximum in density was observed at 1400 °C. The grain size continuously increased with the SPS temperature into the micrometer size range. The maximum in density arises from competition between densification and grain growth. Retarded densification above 1400 °C is associated with enhanced grain growth that resulted in residual pores within the grains. Analysis of the grain growth kinetics resulted in activation energy of 150 kJ mol^{-1} and associated diffusion coefficients higher by 10^3 than expected for Y^{3+} grain boundary diffusion. The enhanced diffusion may be explained by combined surface diffusion and particle coarsening during the heating up with grain boundary diffusion at the SPS temperature.

Keywords: Spark plasma sintering; Nanocrystalline; Y_2O_3; Grain growth; Densification

1. Introduction

Spark plasma sintering (SPS) is a versatile technique used for rapid densification of ceramics at moderate temperatures.[1–4] The rapid sintering and densification in SPS were related to the thermal processes at the free surfaces of the powder particles.[5,6] Therefore, nanocrystalline ceramic powders are the best candidates for densification by SPS and have exhibited improved densification behavior.[7–10] Recently, we have shown that transparent polycrystalline ceramics may be fabricated by SPS, regardless of their high melting temperature (i.e. MgO[11]) or high flow stress (i.e. YAG[12]). Application of SPS in the strictly controlled conditions[13] may result in fully dense transparent oxide ceramics that can be appropriate for optical applications.

Yttrium oxide (Y_2O_3) with cubic symmetry is one of the important oxide hosts for the solid state lasers, as well as for infrared ceramics. Polycrystalline Y_2O_3 was sintered to full density and transparency by different routes.[14–18] It exhibited superplastic behavior above 1300 °C under tensile stresses.[19] Therefore, ultrafine grained Y_2O_3 ceramics may have the benefits of superplastic ability during processing as well as high optical transparency in the annealed conditions. The present work investigated the densification behavior and the microstructure evolution of nanocrystalline Y_2O_3 powder (herein nc-Y_2O_3) subjected to densification at different SPS conditions.

2. Experimental procedures

Ultra-pure (99.99%) nanocrystalline Y_2O_3 (Cathay Advanced Materials, China) with 18 nm mean crystallite size (diameter) was used. Discs of 8 mm diameter and 2 mm thickness were fabricated using the SPS unit (Dr. Sinter, SPS 2080) of the Plateforme Nationale de Frittage Flash (PNF2) du CNRS located at Toulouse. The as-received powders were poured into the graphite die where the die wall and the punch surfaces were shielded using graphite foils. Three different heating rates (50, 100 and 180 °C min^{-1}) were examined. The SPS temperature ranged between 1100 and 1600 °C. The pulsed DC current density up to 200 A cm^{-2} with pulse duration of 3.3 ms was used. The temperature increase to 600 °C over a period of 3 min was controlled by thermocouple; further temperature increase was regulated and monitored by an optical

* Corresponding author. Tel.: +972 4 8294589; fax: +972 4 8295677.
E-mail address: rchaim@technion.ac.il (R. Chaim).

0955-2219/$ – see front matter © 2008 Elsevier Ltd. All rights reserved.
doi:10.1016/j.jeurceramsoc.2008.05.043

pyrometer focused on a small hole located at the surface of the die. Uniaxial pressure of 100 MPa was applied at the SPS temperature for 5 min SPS duration. The vacuum level of 2–3 Pa was maintained during the SPS process.

The final density was measured by the Archimedes method following the ASTM standard C 20–92 with an accuracy of ±0.5% using distilled water medium. The sintered specimens were mechanically polished down to 1 μm using diamond pastes, and thermally etched for 30 min at 1100 °C. Fracture surfaces were also used for grain size statistics, to confirm the data acquired from the polished surfaces. The microstructures of the powder and the sintered specimens were characterized, respectively, using transmission (TEM, Jeol FX2000) and high resolution scanning electron microscopy (HRSEM, Leo Gemini 982, at 4 kV) equipped with X-ray energy dispersive spectroscopy (EDS). About 200 grains were counted in each specimen for the grain size statistics, where the largest axis of the grain was measured.

3. Results

3.1. The as-received powder

The as-received powder was in the form of sub-micrometer size agglomerates composed of nanocrystalline Y_2O_3 (Fig. 1a) with cubic crystal symmetry (JCPDS # 41-1105) (Fig. 1b). The mean crystallite size directly measured from TEM images was 18 ± 8 nm, and exhibited log-normal distribution. A powder compact was prepared by cold isostatic pressing, and its shrinkage behavior was characterized both in a dilatometer and by the SPS runs. These experiments examined the shrinkage of the powder compact at low heating rate (5 °C min^{-1}) and negligible load (in the dilatometer) as well as high heating rate (180 °C min^{-1}) and different loads (2 and 100 MPa in the SPS unit) used further in the SPS experiments. The main shrinkage of the green compact in the dilatometer started around 1000 °C (Fig. 2a) with two maximum shrinkage rates at ∼1300 and ∼1600 °C. The shrinkage in the SPS runs started at 650 °C under 100 MPa and 800 °C under 2 MPa load (Fig. 2b) and continued up to 900 and 1500 °C, respectively. The maximum shrinkage rates were around 750 and 1000 °C, respectively. Therefore, the SPS experiments were performed within the temperature range 1100–1600 °C.

3.2. Effect of heating rate

The effect of heating rate on the densification and grain growth was evaluated using different SPS parameters as shown in Fig. 3. The higher the heating rate and temperature, the larger the final grain size (Fig. 3a), and higher the relative density (Fig. 3b). The highest heating rate of 180 °C min^{-1} was used for further SPS experiments with nc-Y_2O_3.

3.3. Effect of SPS temperature

The effect of SPS temperature on densification and grain growth was evaluated from the density and grain size measurements. The continuous increase in the mean grain size was consistent with the increase in the SPS temperature (Fig. 4). The grain size distribution was also broadened with the increase in the SPS temperature, as was evident from the increase in the standard deviation of the mean grain size in Fig. 4. However, the relative density increased with the SPS temperature up to 1400 °C, followed by a significant decrease at higher temperatures. These changes of a few percent in the relative density are much higher than the standard deviation of the relative density (±0.5%), and thus indicates the change in the densification rate with temperature. Nevertheless, all the relative densities are above 93%, which is consistent with the presence of closed porosity within the sintered specimens.

Following the linear shrinkage curves versus temperature, the main shrinkage in the specimens took place during the heating stage after ∼320–330 s between 950 and 1050 °C, irrespective of their final SPS temperatures (Fig. 5). Therefore, the additional 5 min duration at the SPS temperature should be associated with

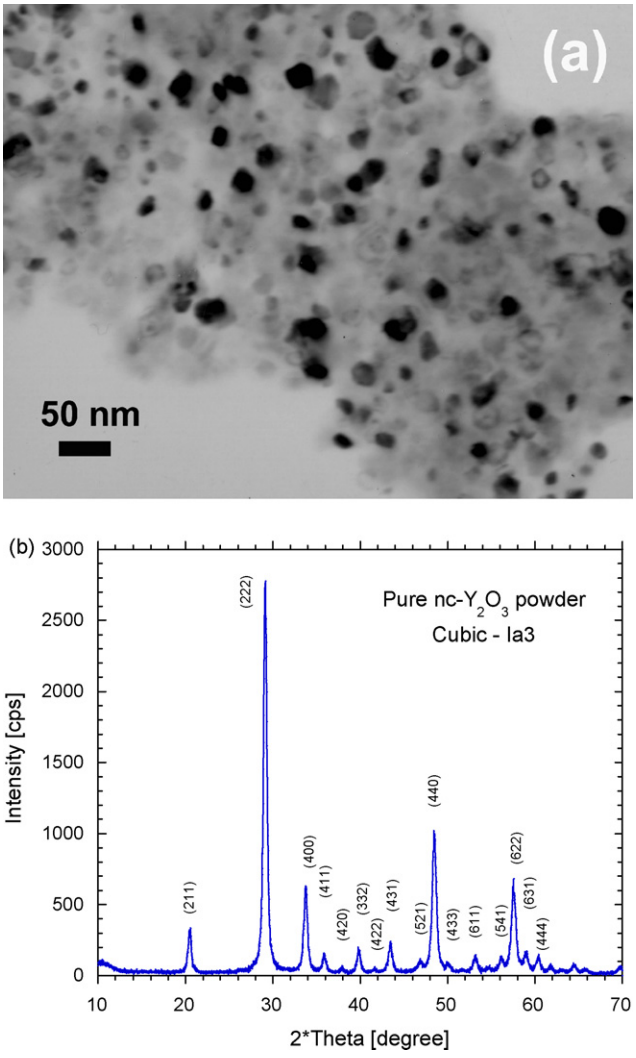

Fig. 1. (a) Bright-field TEM image showing the Y_2O_3 nanocrystallites agglomerated as sub-micrometer powder particles. (b) X-ray diffraction spectrum showing the Y_2O_3 cubic symmetry.

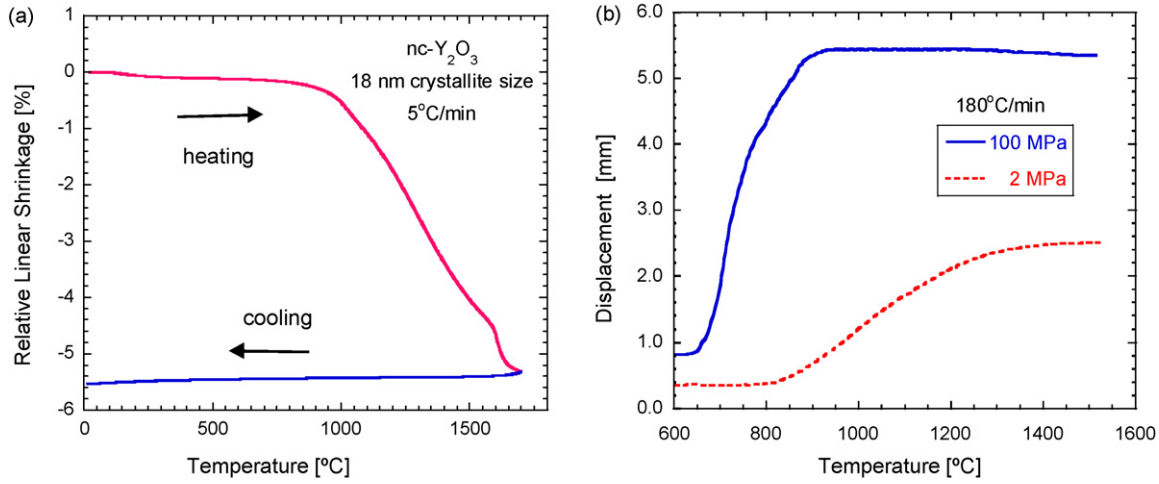

Fig. 2. Linear shrinkage of nc-Y_2O_3 powder compact in (a) dilatometer at 5 °C min^{-1} heating rate. (b) SPS under 2 and 100 MPa load and high heating rate of 180 °C min^{-1}.

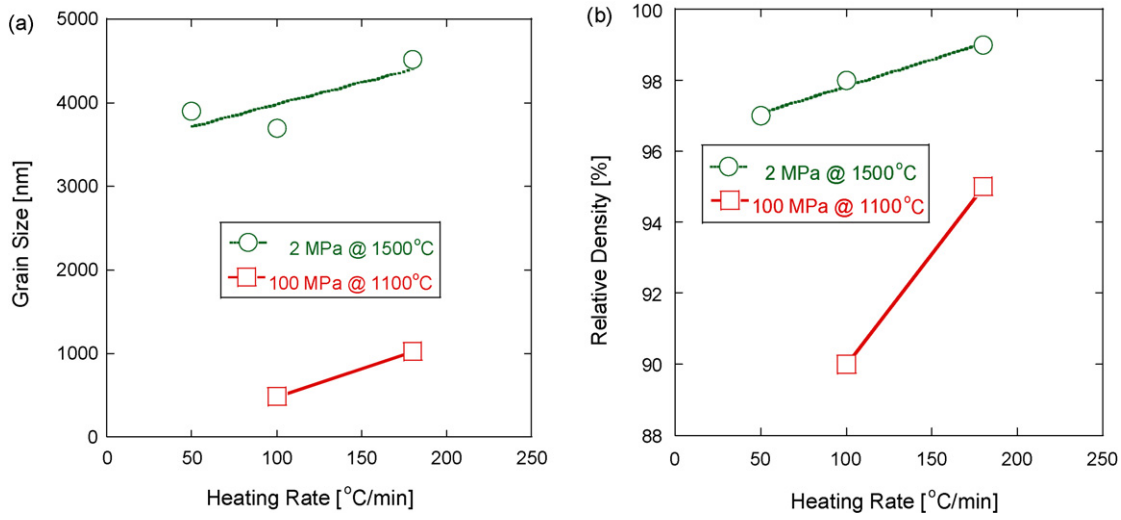

Fig. 3. Effect of heating rate at different SPS pressures and temperatures on the (a) grain size and (b) relative density of nc-Y_2O_3.

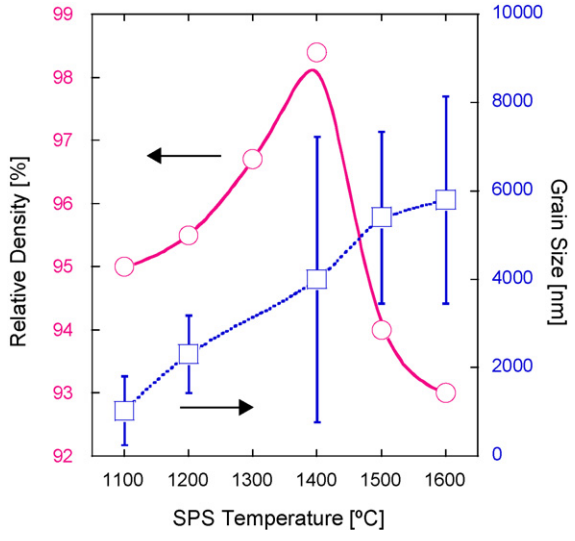

Fig. 4. Relative density and average grain size versus the SPS temperature for 5 min and 100 MPa, using the heating rate 180 °C min^{-1}.

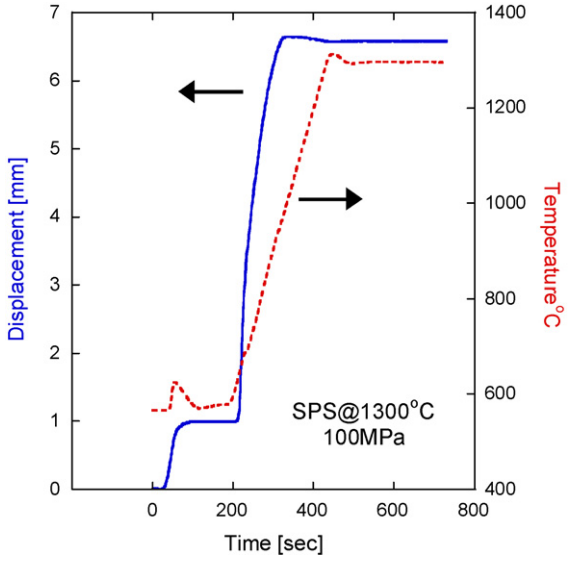

Fig. 5. Displacement versus temperature showing that the main shrinkage takes place after ~320 s around 950 °C.

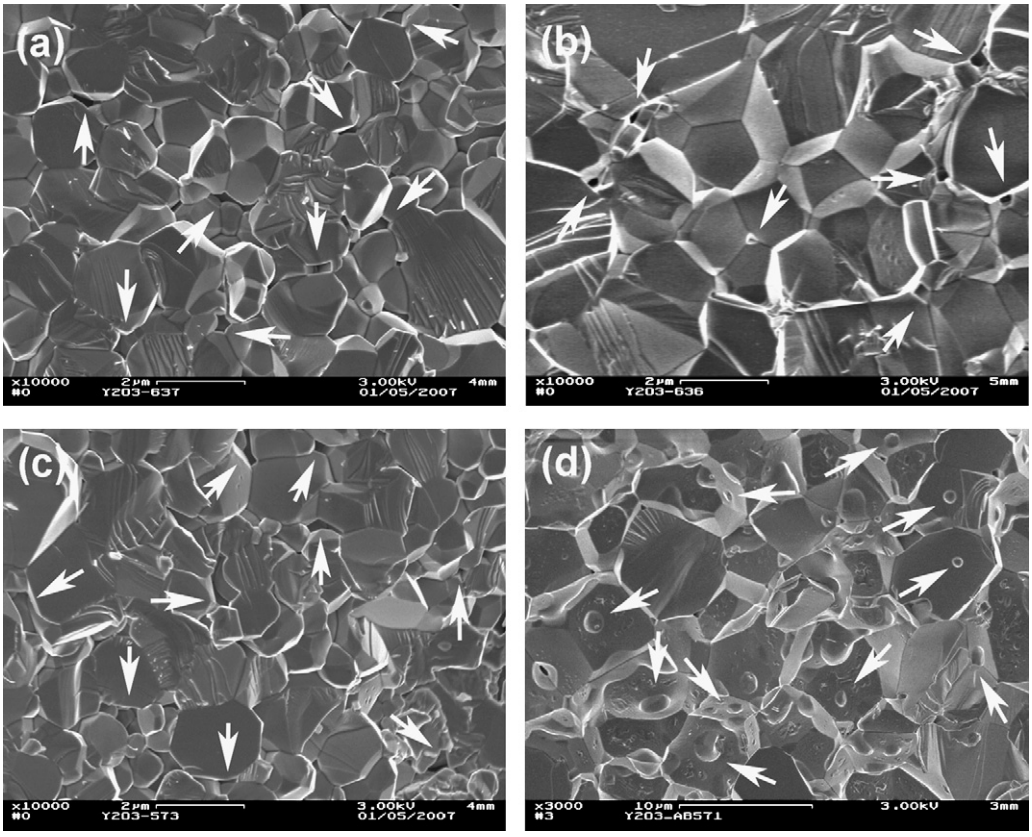

Fig. 6. SEM images from the fracture surfaces of Y_2O_3 specimens after SPS at (a) 1100 °C, (b) 1200 °C, (c) 1300 °C, (d) 1400 °C. The pores at the grain junctions in (a) to (c) and on grain boundaries in (d) were arrowed.

further densification into the final stage of sintering (i.e. relative density above 90%) and grain growth.

3.4. Grain growth

The fracture surface of the Y_2O_3 specimens exhibited homogeneous microstructures with equiaxed polyhedral shape grains (Fig. 6). At SPS temperatures below 1400 °C (Fig. 6a and b) the planar and exposed grain boundary surfaces were pore-free; a few residual pores were located at the grain junctions such as triple-points and quadruple nodes (arrowed). On the other hand, the traces of the residual pores located at the exposed grain boundary surfaces increased with the increase in the SPS temperature above 1400 °C (arrowed in Fig. 6d). Electron microscopy of the specimens after SPS at the highest temperatures (i.e. 1500 and 1600 °C) also showed large residual pores in the grain interiors (arrowed in Fig. 7). The latter pores were also visible using HRSEM and their content increased with temperature.

In order to reveal the active densification and associated grain growth mechanisms during the SPS of nc-Y_2O_3, the grain size data were analyzed using the general grain growth equation. Grain growth by different atomistic mechanisms can be expressed using the equation:

$$G_t^n - G_0^n = Kt \tag{1}$$

where

$$K = K_0 \exp\left(-\frac{Q}{RT}\right) \quad [\mathrm{m^2\,s^{-1}}] \tag{2}$$

where G_t and G_0 are the grain sizes at time t and $t=0$, respectively, n is the grain growth exponent, K_0 is the pre-exponential constant of the diffusion coefficient, Q is the activation energy for grain growth, T is the absolute temperature, and R is the gas constant.

The value of the grain growth exponent characterizes the rate controlling process, $n=2$ for grain growth controlled by grain boundary diffusion, $n=4$ for particle coarsening by surface diffusion, versus $n=3$ for grain growth controlled either by diffusion through the lattice or through a liquid phase at the grain boundary. The grain size data (Fig. 4) were analyzed according to Eqs. (1) and (2), and the resultant Arrhenius plots are shown in Fig. 8; the data exhibited high degree of fit to three lines ($R=0.9915$ for $n=2$, and $R=0.9930$ for $n=3$ in Fig. 8a, and $R=0.9945$ for $n=4$ in Fig. 8b). The corresponding activation energies derived from the line slopes were 150, 230, and 311 kJ mol^{-1} for $n=2$, 3 and 4, respectively. In order to confirm or negate either of the densification mechanisms mentioned above, attempt was made to evaluate the diffusion coefficients that correspond to the observed grain growth. Following our microstructural observations, density and grain size measurements, some deductions and assumptions can be made towards

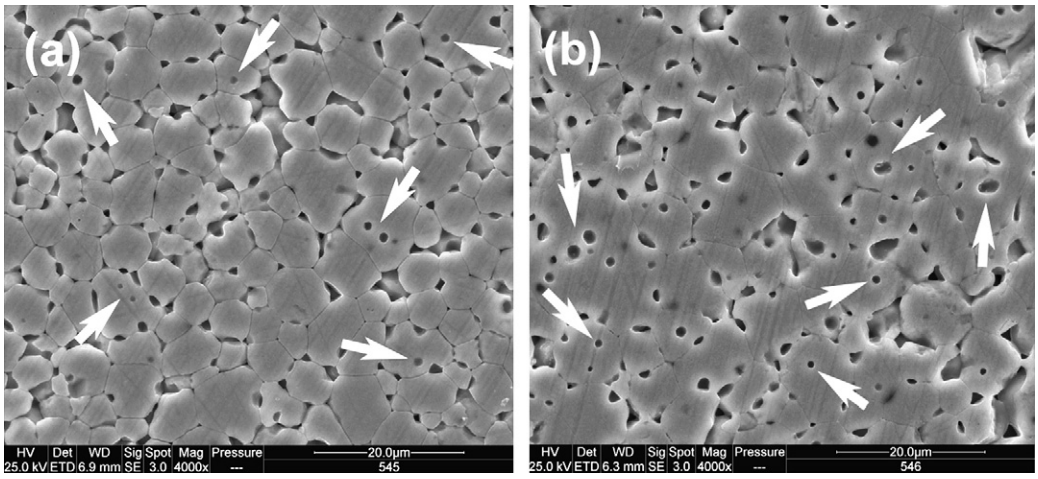

Fig. 7. SEM images from the polished and chemically etched Y_2O_3 specimens after SPS at (a) 1500 °C, and (b) 1600 °C. The residual pores located at the grain boundaries and within the grains, the latter were arrowed.

this evaluation process. Based on Fig. 5, the main shrinkage was observed during the heating stage. Therefore, the available free surface is negligible at the SPS temperature for contributing to the grain growth/coarsening via surface diffusion. In addition, the rapid grain growth at temperatures below 1400 °C and the presence of entrapped pores within the grains above 1400 °C both in favor of grain boundary diffusion compared to lattice diffusion. Therefore, the main grain growth at the SPS temperature was assumed to take place by normal grain growth and controlled by grain boundary diffusion, i.e. $n = 2$. The time constant, K, is given by:

$$K = 2\alpha\gamma_{gb}M_{gb} \tag{3}$$

where α is a geometrical factor (~1.5) and γ_{gb} is the grain boundary energy (~0.5 J m^{-2}). The grain boundary mobility, M_{gb} is given by[20]:

$$M_{gb} = \frac{D_{gb}^{\perp}}{RT}\left(\frac{\Omega}{\delta_{gb}}\right) \tag{4}$$

where $D_{gb}^{\perp}$ is the diffusion coefficient of the slower ionic species perpendicular to the grain boundary, Ω is the transported volume for one atom of the controlling species, and δ_{gb} is the grain boundary thickness.

Substituting from Eqs. (3) and (4) into (1), the diffusion coefficient can be evaluated using the grain growth data. The present activation energies and the corresponding diffusion data from the grain growth kinetics were compared to those from the literature as will be discussed below.

4. Discussion

Possible densification mechanisms for the ceramic nanoparticle compacts during the SPS were previously described.[1,21–24] The active densification mechanism was found to depend on

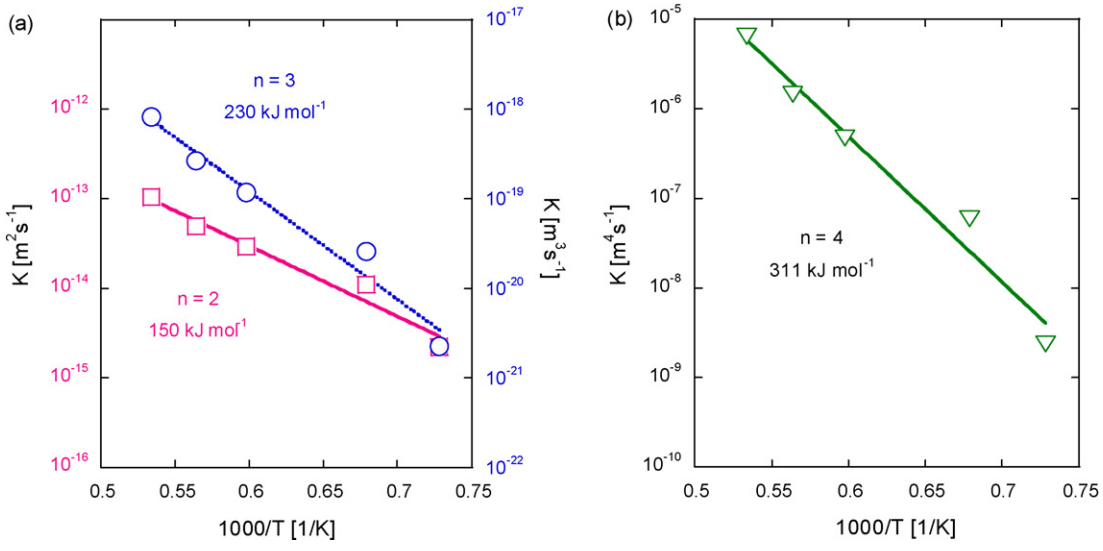

Fig. 8. Arrhenius plots for $n = 2$–4 and their corresponding activation energies.

the change in both the mechanical and electrical properties with temperature. In this respect, densification of the green compact may proceed by two competitive processes: time-independent deformation by plastic yield of the particles versus time-dependent deformation/mass transport by diffusional processes. Diffusional plastic deformation processes may proceed by sliding of the grains over each other aided by surface diffusion at lower temperatures and relative densities. Indications for densification via particle surface softening were also reported for nanocrystalline yttrium aluminum garnet.[12] At higher temperatures and densities, grain deformation via creep aided by grain boundary/volume diffusion is more probable. In addition, due to the nanocrystalline nature of the Y_2O_3 powder, particle coarsening during the heating up and at densities below ~90% as well as grain growth at the SPS temperature and at densities above ~90% should be taken into account.

Plastic yield of the ceramic particles/grains may take place above a certain temperature where dislocation slip systems become active. Plastic deformation of Y_2O_3 single crystals[25] and polycrystals[19,26] at high temperatures was investigated, where continuous brittle–ductile transition was observed above 1000 °C (Fig. 9). Compression as well as tensile tests of highly pure polycrystalline Y_2O_3 between 1200 and 1800 °C confirmed that the yield stress decreases with the decrease in the grain size as shown in Fig. 9. Superplastic-like behavior was observed in hot-pressed Y_2O_3 with sub-micrometer grain size.[19] At pressures below 20 MPa, creep was found to be viscous, while at higher stresses a power-law creep was observed. Nevertheless, the creep rates were negligibly low, 10^{-6} s^{-1} and therefore cannot account for the extensive densification.

Recalling the applied pressure of SPS as 100 MPa, the contribution of plastic yield to densification at SPS temperatures below 1400 °C may be negligible. This was confirmed by dislocation-free grains observed in TEM images (not shown here). Therefore, the contribution of the diffusional processes to densification should be considered.

Mass transfer in ceramic oxides is associated with ambipolar diffusion to satisfy the need for charge neutrality. Different types of experiments were conducted to determine the various diffusion coefficients of Y^{3+} cations and O^{2-} anions along the grain boundaries and within the lattice, using single crystal[27–29] and polycrystalline specimens.[30–34] Significant scatter in the diffusion coefficient data exists in these published results, especially with polycrystalline Y_2O_3, mainly due to porosity, impurity, and grain size effects. The results of the single crystal diffusion experiments may be accounted for by lattice diffusion of the corresponding ions, since no interference with surface or grain boundary diffusion may be encountered. The corresponding lattice diffusion coefficients for O^{2-} [28] and Y^{3+} [29] are:

$$D^{O}_{Lattice} = 7.3 \times 10^{-10}[m^2\,s^{-1}] \exp\left(-\frac{191[kJ\,mol^{-1}]}{RT}\right) \quad (1100 - 1500\,^{\circ}C) \tag{5a}$$

$$D^{Y}_{Lattice} = 3.5 \times 10^{-9}[m^2\,s^{-1}] \exp\left(-\frac{343[kJ\,mol^{-1}]}{RT}\right) \quad (1600 - 1700\,^{\circ}C) \tag{5b}$$

These diffusion coefficients were plotted versus inverse temperature (filled symbols in Fig. 10) and clearly reveal the lower values for Y^{3+} compared to O^{2-}. Consequently, Y^{3+} is the rate controlling specie during the ambipolar diffusion, hence the rest of the diffusion data in Fig. 10 are referred to the cation. We analyzed the published grain boundary mobility data for pure Y_2O_3[33] in terms of the diffusion coefficients via Eq. (4) (open triangles in Fig. 10). Good agreement was found with Y^{3+} lattice diffusion coefficients (filled triangles in Fig. 10), albeit different activation energies with high scatter were reported.[29,33] This finding can be rationalized when the grain boundary mobility is controlled by lattice diffusion of the controlling species towards the space charge layer at the grain boundary, as in

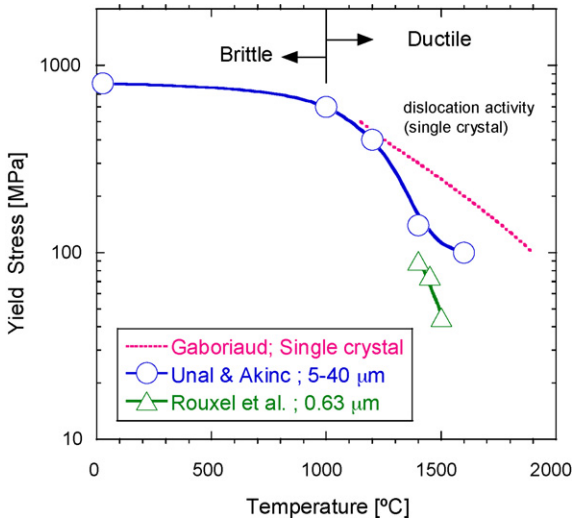

Fig. 9. Yield stress of single crystal and polycrystalline Y_2O_3 versus temperature showing the temperatures range of brittle to ductile transition (refs. 19,25,26).

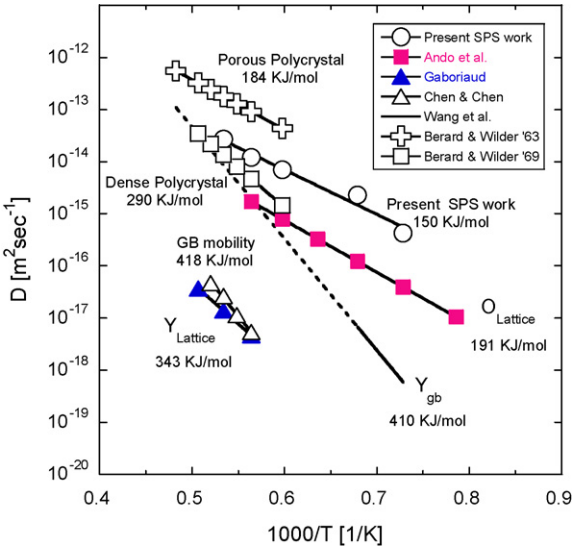

Fig. 10. Diffusion coefficients of Y^{3+} and O^{2-} in Y_2O_3 (refs. 27–31,33–34).

the case of solute drag mechanism perpendicular to the grain boundary (doped-Y_2O_3 was used in ref. 33). Cation diffusion in polycrystalline Y_2O_3 was carried out in specimens differing in their grain size as well as final density.[30,31] The 99.9% dense specimens with 18 μm average grain size[30] exhibited diffusion coefficients (open squares in Fig. 10) lower by one to two orders of magnitude compared to their counterparts from 94 to 97% dense specimens with 36 μm average grain size[31] (open crosses in Fig. 10). Where the diffusion coefficients in the porous specimens included combined grain boundary and surface diffusion (along the pore surfaces), the lower values in the fully dense specimens may be related to Y^{3+} along the grain boundaries. The latter assumption may be supported by the Y^{3+} grain boundary diffusion coefficient data deduced from two-step sintering studies of Y_2O_3.[34] Although limited in their temperature range (1100–1200 °C), extrapolation of these results to higher temperature (dashed line in Fig. 10) tends to result in similar values as in dense polycrystalline Y_2O_3. Finally, the calculated diffusion coefficients from the present SPS work (open circles in Fig. 10) are in good agreement with those from dense polycrystalline Y_2O_3 (open squares in Fig. 10) at high temperatures only (∼1700 °C). They depart from each other with the temperature decrease, up to three orders of magnitude difference at 1100 °C.

Based on the data presented in Fig. 10, diffusion of Y^{3+} along the grain boundaries can be considered as a main atomistic mechanism that controls the densification and grain growth during the SPS of nanocrystalline Y_2O_3. In addition, surface diffusion may also contribute to particle coarsening during the heating up. We analyzed the grain size data reported during coarsening of nanocrystalline Y_2O_3 powders in the temperature range 900–1100 °C[35] from which activation energy of 170 kJ mol^{-1} was determined. Since the vapor pressure of yttria is very low below 1000 °C,[36] evaporation–condensation may be negated, and this activation energy should be related to surface diffusion as the dominant mechanism for particle coarsening. This calculated value is an intermediate between the activation energy from our SPS results (150 kJ mol^{-1}) and that from diffusion in porous polycrystals (184 kJ mol^{-1}). It was shown above, that all the specimens reached the final stage of sintering (i.e. 90% density) during the heating stage, around ∼1000 °C. Therefore, surface diffusion is active during part of the densification process.

Finally, the lower densities observed above 1400 °C should be related to the competition between densification and grain growth. As was mentioned above, all the specimens reached the final stage of sintering (i.e. 90% density) during the heating stage, around ∼1000 °C. The transition from the intermediate to the final stage of sintering is characterized by the conversion of the continuous pores into isolated pores. Since the isolated pores are by far less efficient in pinning the grain boundaries, compared to the continuous pores, enhanced grain growth takes place at the final stage of sintering. As long as the pore mobility is greater than/equal to the grain boundary mobility, the pore is dragged by the migrating grain boundary and is consumed via vacancy diffusion along the grain boundaries. However, at temperatures high enough (i.e. >1400 °C), when the grain boundary mobility may become higher than the pore mobility, the pore may be detached from the grain boundary and left within the grains, as was observed for the high SPS temperatures (Fig. 7). Such occluded pores may shrink only by lattice diffusion, towards their neighbor grain boundary—a slower mechanism than grain boundary diffusion. Consequently, this competition between densification by the isolated pore shrinkage and grain growth leads to optimal SPS temperature for full densification.

5. Summary and conclusions

Nanocrystalline Y_2O_3 powders were densified to fully dense specimens by SPS for 5 min at 100 MPa in the temperature range 1100–1600 °C. Increase in the heating rate up to 180 °C min^{-1} led to increase in both density and grain size. While continuous grain growth was observed with the increase in the SPS temperature, a maximum in density was observed at 1400 °C. Based on the microstructure observations this maximum is due to competition between densification and enhanced grain growth; the latter dominating above 1400 °C. Analysis of the grain growth kinetics and its associated diffusion coefficients and activation energy was in agreement with particle coarsening during the heating up stage, followed by grain boundary diffusion at the SPS temperature. The Y^{3+} grain boundary diffusion coefficients were enhanced by three orders of magnitude compared to the literature data.

Acknowledgments

The financial support of the Israel Ministry of Defense and the Israel Ministry of Science are gratefully acknowledged. The authors thank G. Raimbeaux for the help in the SPS experiments.

References

1. Tokita, M., Mechanism of spark plasma sintering and its application to ceramics. *Nyu Seramikkusu (New Ceram.)*, 1997, **10**, 43–53 [in Japanese].
2. Mishra, R. S., Risbud, S. H. and Mukherjee, A. K., Influence of initial crystal structure and electrical pulsing on densification of nanocrystalline alumina powder. *J. Mater. Res.*, 1998, **13**, 86–89.
3. Nygren, M. and Shen, Z., On the preparation of bio-, nano- and structural ceramics and composites by spark plasma sintering. *Solid State Sci.*, 2003, **5**, 125–131.
4. Harada, Y., Uekawa, N., Kojima, T. and Kakegawa, K., Fabrication of $Y_3Al_5O_{12}$–Al_2O_3 eutectic materials having ultra fine microstructure. *J. Eur. Ceram. Soc.*, 2008, **28**, 235–240.
5. Groza, J. R. and Zavaliangos, A., Sintering activation by external electrical field. *Mater. Sci. Eng. A*, 2000, **287**, 171–177.
6. Wang, S. W., Chen, L. D. and Hirai, T., Densification of Al_2O_3 powder using spark plasma sintering. *J. Mater. Res.*, 2000, **15**, 982–987.
7. Li, W. and Gao, L., Rapid sintering of nanocrystalline ZrO_2 (3Y) by spark plasma sintering. *J. Eur. Ceram. Soc.*, 2000, **20**, 2441–2445.
8. Wang, L., Jiang, W. and Chen, L., Rapidly sintering nanosized SiC particle reinforced TiC composites by the spark plasma sintering (SPS) technique. *J. Mater. Sci.*, 2004, **39**, 4515–4519.
9. Chaim, R., Superfast densification of nanocrystalline oxide powders by spark plasma sintering. *J. Mater. Sci.*, 2006, **41**, 7862–7871.
10. Anselmi-Tamburini, U., Garay, J. E. and Munir, Z. A., Fast low-temperature consolidation of bulk nanometric ceramic materials. *Scr. Mater.*, 2006, **54**, 823–828.
11. Chaim, R., Shen, Z. and Nygren, M., Transparent nanocrystalline MgO by rapid and low-temperature spark plasma sintering. *J. Mater. Res.*, 2004, **19**, 2527–2531.

12. Chaim, R., Marder-Jeackel, R. and Shen, J. Z., Transparent YAG ceramics by surface softening of nanoparticles in spark plasma sintering. *Mater. Sci. Eng. A*, 2006, **429**, 74–78.
13. Chesnaud, A., Bogicevic, C., Karolak, F., Estournes, C. and Dezanneau, G., Preparation of transparent oxyapatite ceramics by combined use of freeze-drying and spark-plasma sintering. *Chem. Commun. (Cambridge, United Kingdom)*, 2007, **15**, 1550–1552.
14. Chen, P.-L. and Chen, I.-W., Sintering of fine oxide powders: II. Sintering mechanisms. *J. Am. Ceram. Soc.*, 1997, **80**, 637–645.
15. Saito, N., Matsuda, S.-I. and Ikegami, T., Fabrication of transparent yttria ceramics at low temperature using carbonate-derived powder. *J. Am. Ceram. Soc.*, 1998, **81**, 2023–2028.
16. Ikegami, T., Mori, T., Yajima, Y., Takenouchi, S., Misawa, T. and Moriyoshi, Y., Fabrication of transparent yttria ceramics through the synthesis of yttrium hydroxide at low temperature and dopping by sulfate ions. *J. Ceram. Soc. Japan*, 1999, **107**, 297–299.
17. Wen, L., Sun, X., Lu, Q., Xu, G. and Hu, X., Synthesis of yttria nanopowders for transparent yttria ceramics. *Opt. Mater.*, 2006, **29**, 239–245.
18. Eilers, H., Fabrication, optical transmittance, and hardness of IR-transparent ceramics made from nanophase yttria. *J. Eur. Ceram. Soc.*, 2007, **27**, 4711–4717.
19. Rouxel, T., Murat, D., Besson, J. L. and Boncoeur, M., Large tensile ductility of high purity polycrystalline yttria. *Acta Mater.*, 1996, **44**, 263–278.
20. Rahaman, M. N., *Ceramic Processing and Sintering*. Marcel Dekker Inc., New York, 2003, p. 600.
21. Mamedov, V., Spark plasma sintering as advanced PM sintering method. *Powder Metall.*, 2002, **45**, 322–328.
22. Chaim, R. and Margulis, M., Densification maps for spark plasma sintering of nanocrystalline MgO ceramics. *Mater. Sci. Eng. A*, 2005, **407**, 180–187.
23. Olevsky, E. and Froyen, L., Constitutive modeling of spark plasma sintering of conductive materials. *Scr. Mater.*, 2006, **55**, 1175–1178.
24. Chaim, R., Densification mechanisms in spark plasma sintering of nanocrystalline ceramics. *Mater. Sci. Eng. A*, 2007, **443**, 25–32.
25. Gaboriaud, R. J., Fluage haute temperature du sesquioxyde d'yttrium: Y_2O_3. *Philos. Mag. A*, 1981, **44**, 561–587 [in French].
26. Unal, O. and Akinc, M., Compressive properties of yttrium oxide. *J. Am. Ceram. Soc.*, 1996, **79**, 805–808.
27. Berard, M. F., Wirkus, C. D. and Wilder, D. R., Diffusion of oxygen in selected monocrystalline rare earth oxides. *J. Am. Ceram. Soc.*, 1968, **51**, 643–647.
28. Ando, K., Oishi, Y., Hase, H. and Kitazawa, K., Oxygen self-diffusion in single-crystal Y_2O_3. *J. Am. Ceram. Soc.*, 1983, **66**, C222–C223.
29. Gaboriaud, R. J., Self-diffusion of yttrium in monocrystalline yttrium oxide: Y_2O_3. *J. Solid State Chem.*, 1980, **35**, 252–261.
30. Berard, M. F. and Wilder, D. R., Self-diffusion in polycrystalline yttrium oxide. *J. Appl. Phys.*, 1963, **34**, 2318–2321.
31. Berard, M. F. and Wilder, D. R., Cation self-diffusion in polycrystalline Y_2O_3 and Er_2O_3. *J. Am. Ceram. Soc.*, 1969, **52**, 85–88.
32. Sordelet, D. J. and Akinc, M., Sintering monosized spherical yttria powders. *J. Am. Ceram. Soc.*, 1988, **71**, 1148–1153.
33. Chen, P.-L. and Chen, I.-W., Grain boundary mobility in Y_2O_3: defect mechanism and dopant effects. *J. Am. Ceram. Soc.*, 1996, **79**, 1801–1809.
34. Wang, X.-H., Chen, P.-L. and Chen, I.-W., Two-step sintering of ceramics with constant grain-size, I. Y_2O_3. *J. Am. Ceram. Soc.*, 2006, **89**, 431–437.
35. Huang, Z., Sun, X., Xiu, Z., Chen, Sh. and Tsai, C.-T., Precipitation synthesis and sintering of yttria nanopowders. *Mater. Lett.*, 2004, **58**, 2137–2142.
36. Ikegami, T., Li, J.-G., Mori, T. and Moriyoshi, Y., Fabrication of transparent yttria ceramics by the low-temperature synthesis of yttrium hydroxide. *J. Am. Ceram. Soc.*, 2002, **85**, 1725–1729.